

# $\mu$ GUIDE: a framework for microstructure imaging via generalized uncertainty-driven inference using deep learning

Maëliss Jallais<sup>1,2</sup> and Marco Palombo<sup>1,2</sup>

<sup>1</sup> Cardiff University Brain Research Imaging Centre (CUBRIC), School of Psychology, Cardiff University, Cardiff, United Kingdom;

<sup>2</sup> School of Computer Science and Informatics, Cardiff University, Cardiff, United Kingdom

## Abstract

This work proposes  $\mu$ GUIDE: a general Bayesian framework to estimate posterior distributions of tissue microstructure parameters from any given biophysical model or MRI signal representation, with exemplar demonstration in diffusion-weighted MRI. Harnessing a new deep learning architecture for automatic signal feature selection combined with simulation-based inference and efficient sampling of the posterior distributions,  $\mu$ GUIDE bypasses the high computational and time cost of conventional Bayesian approaches and does not rely on acquisition constraints to define model-specific summary statistics. The obtained posterior distributions allow to highlight degeneracies present in the model definition and quantify the uncertainty and ambiguity of the estimated parameters.

## 1 Introduction

Diffusion-weighted MRI (dMRI) is a promising technique for characterizing brain microstructure in-vivo using a paradigm called microstructure imaging [Novikov et al., a, Alexander et al., Jelescu et al., b]. Traditionally, microstructure imaging quantifies histologically meaningful features of brain microstructure by defining a forward (biophysical) model to link the model parameters to measured dMRI signal. These tissue microstructure parameters are then inferred by fitting the biophysical model voxel-wise to the set of signals obtained from images acquired with different sensitivities, yielding model parameter maps [Alexander et al.].

Most commonly used techniques rely on a non-linear curve fitting of the signal and return the optimal solution, i.e. the best parameters guess of the fitting procedure. However, these methods only return one possible combination of model parameters that could explain an observed signal and hide model degeneracy, that is all the other possible estimates [Jelescu et al., c]. To address this degeneracy problem, a first approach is to increase the amount of information contained in the signal that is fed to the fitting procedure by, for example, varying some acquisition parameters such as the echo time [Veraart et al., c, Gong et al., Palombo et al., b, De Almeida Martins et al., Slator et al.] or the diffusion time [Jespersen et al., Jelescu et al., a, Warner et al., Uhl et al., Mougél et al.], using very strong multi-directional diffusion encoding [Veraart et al., a, Olesen et al., Palombo et al., a, Howard et al., Jones et al.] or adding "orthogonal" acquisitions such as double diffusion encoding [Vincent et al., Henriques et al., Afzali et al., Lampinen et al., a,b]. However, this solution might not always be doable in clinical settings or practice as it requires advanced sequences and it leads to longer acquisition times and increased costs. Multiple strategies have therefore been proposed to deal with the degeneracy problem for a given acquisition and biophysical model. Some methods suggest to remove the degeneracy arising from the model definition by imposing additional constraints on the parameters or fixing them to predetermined values, chosen according to physical principles and current knowledge [Fieremans et al., a, Zhang et al.]. However, the biophysical validity of such constraints may be questionable in some conditions [Novikov et al., b], potentially introducing bias, for example in pathological tissue evaluations [Novikov et al., a, Lampinen et al., d,c]. Another alternative is optimizing the machine learning training dataset to eliminate degenerate parameter combinations [Guerreri et al., Gyori et al.]. Other works propose different strategies for selecting the preferred solution [Novikov et al., b, Fieremans et al., b]. This selection is nontrivial, since the multiple parameter sets often appear equally biophysically plausible. An erroneous choice of parameters can significantly alter the

interpretation and diagnostic implications of the estimated parameters. Instead of attempting to remove the degeneracies, we propose to highlight them and present all the possible parameter values that could explain an observed signal, providing users with more information to make more confident and explainable use of the inference results.

Another crucial consideration in model fitting is accounting for the uncertainty in parameter estimates. This uncertainty serves various purposes, including assessing result confidence [Jones], quantifying noise effects [Behrens et al.] or assisting in experimental design [Alexander, a]. Gradient descent often provides a measure of confidence for each parameter estimate. Alternative approaches use the shape of the fitted tensor itself as a measure of uncertainty for the fiber direction [Koch et al., Parker and Alexander]. Other methods also rely on bootstrapping techniques to estimate uncertainty. Repetition bootstrapping for example depends on repeated measurements of signal for each gradient direction, but imply a long acquisition time and cost, and are prone to motion artifacts [Lazar and Alexander, Jones]. In contrast, residual bootstrapping methods resample the residuals of a regression model. Yet, this approach is heavily dependent on the model and can lead to overfitting [Whitcher et al., Chung et al.]. In general, resampling methods can be problematic for sparse samples, as the bootstrapped samples tend to underestimate the true randomness of the distribution [Kauermann et al.].

Posterior distributions are powerful tools to characterize all the possible parameter estimations that could explain an observed measurement, their uncertainty, and existing model degeneracy [Box and Tiao]. Bayesian inference allows for the estimation of these posterior distributions, via the definition of two quantities: the prior distribution, which encodes our initial knowledge of the parameter values; and the likelihood function of the forward model being studied.

To approximate these posterior distributions, traditional methods rely on the estimation of the likelihood  $p(\mathbf{x}|\boldsymbol{\theta})$  of the observed data point  $\mathbf{x}$  via an analytic expression. This likelihood function corresponds to an integral over all possible trajectories through the latent space, that is  $p(\mathbf{x}|\boldsymbol{\theta}) = \int p(\mathbf{x}, \mathbf{z}|\boldsymbol{\theta})d\mathbf{z}$ , where  $p(\mathbf{x}, \mathbf{z}|\boldsymbol{\theta})$  is the joint probability density of observed data  $\mathbf{x}$  and latent variables  $\mathbf{z}$ . For forward models with large latent spaces, computing this integral explicitly becomes impractical. The likelihood function is then intractable, rendering these methods unusable [Cranmer et al., a].

To circumvent this issue, some techniques have been proposed to sample numerically from the likelihood function, such as Markov-Chain-Monte-Carlo (MCMC) methods [Metropolis et al., Gilks et al., Gamerman and Lopes]. In quantitative MRI, these methods have been used for example to estimate brain connectivity [Behrens et al.], optimize imaging protocols [Alexander, a], or infer crossing fibers by combining multiple spatial resolutions [Sotiropoulos et al.]. However, the need to call the forward model for each studied sample makes these classical Bayesian inference methods computationally expensive and time consuming. It also often requires adjustments and tuning specific to each biophysical model, such as the choice of burn-in length, thinning and the number of samples to store. Some open source packages, such as the Microstructure Diffusion Toolbox (MDT) [Harms and Roebroek], propose a GPU implementation of MCMC with pre-optimized parameters for various models, allowing to reduce the computation time (e.g., from days to hours for analysing a typical dMRI dataset).

Another set of approaches proposes to train a conditional density estimator to learn a surrogate of the likelihood distribution [Papamakarios et al., c, Lueckmann et al., a], the likelihood-ratio [Cranmer et al., b, Gutmann et al., Hermans et al.] or the posterior distribution [Papamakarios and Murray, Lueckmann et al., c, Papamakarios et al., c], allowing to greatly reduce computation times. These methods are dubbed Likelihood-Free Inference (LFI), or Simulation-Based Inference (SBI) methods [Cranmer et al., a, Tejero-Cantero et al.]. In particular, there has been a growing interest towards deep generative modeling approaches in the machine learning community [Lueckmann et al., b]. They rely on specially tailored neural network architectures to approximate probability density functions from a set of examples. Normalizing flows [Papamakarios et al., a] are a particular class of such neural networks that have demonstrated promising results for SBI in different research fields [Gonçalves et al., Greenberg et al., Bittner et al.]. In the dMRI community, the use of SBI methods to characterize full posterior distributions as well as quantify the uncertainty in parameter estimations was first introduced in [Jallais et al., b] for a grey matter model. An application to crossing fibers has recently been proposed by [Karimi et al.].

A challenge when dealing with data like dMRI is to handle their high-dimensionality. As the dimensionality of the data grows, the complexity of the corresponding inverse problem also increases, leading to longer computation times. To address this issue, recent machine learning methods have been developed to accelerate posterior distribution estimation by relying on the definition of summary statistics [Blum et al., Chen et al.]. These summary statistics are features that capture the essential information within a signal, allowing to reduce the size of the input signal.

However, in the dMRI field, these summary statistics are manually designed, model-specific, not easy to define and rely on specific acquisition requirements [Novikov et al., b, Jallais et al., b].

Harnessing a new deep learning architecture for automatic signal feature selection and efficient sampling of the posterior distributions, here we propose  $\mu$ GUIDE: a general Bayesian framework to estimate posterior distributions of tissue microstructure parameters from any given biophysical model/signal representation.  $\mu$ GUIDE extends and generalises previous work [Jallais et al., b] to any forward model and without acquisition constraints, providing fast estimations of posterior distributions voxel-wise. We demonstrate  $\mu$ GUIDE using numerical simulations on three biophysical models of increasing complexity and degeneracy and compare the obtained estimates with existing methods, including the conventional MCMC approach. We then apply the proposed framework to dMRI data acquired from healthy human volunteers and participants with epilepsy.  $\mu$ GUIDE framework is agnostic to the origin of the data and the details of the forward model, so we envision its usage and utility to perform Bayesian inference of model parameters also using data from other MRI modalities (e.g. relaxation MRI) and beyond.

## 2 Theory

### 2.1 Solving the inverse problem using Bayesian inference

#### 2.1.1 The inference problem

We make the hypothesis that an observed dMRI signal  $\mathbf{x}_0$  can be explained (and generated) using a handful of relevant tissue microstructure parameters  $\boldsymbol{\theta}_0$ , following the definition of a forward model:

$$\mathbf{x}_0 = \mathcal{M}(\boldsymbol{\theta}_0)$$

The objective is, given this observation  $\mathbf{x}_0$ , to estimate the parameters  $\boldsymbol{\theta}_0$  that generated it.

Forward models are designed to mimic at best a given biophysical phenomenon, for some given time and scale [Alexander, b, Yablonskiy and Sukstanskii, Jelescu and Budde, Novikov et al., a, Alexander et al., Jelescu et al., b]. As a consequence, forward models are injection functions (every biologically plausible  $\boldsymbol{\theta}_i$  generates exactly one signal  $\mathbf{x}_i$ ), but do not always happen to be bijections, meaning that multiple  $\boldsymbol{\theta}_i$  can generate the same signal  $\mathbf{x}_i$ . It can be impossible, based on biological considerations, to infer which solution  $\boldsymbol{\theta}_i$  best reflects the probed structure. We refer to these models as 'degenerate models'.

Point estimates algorithms, such as minimum least square or maximum likelihood estimation algorithms, allow to estimate one set of microstructure parameters that could explain an observed signal. In the case of degenerate models, the solution space can be multi-modal and those algorithms will hide possible solutions. When considering real-life acquisitions, i.e. noisy and/or under-sampled acquisitions, one also needs to consider the bias introduced with respect to the forward model, and the resulting variance in the estimates [Jones, Behrens et al.].

We propose a new framework that allows for the estimation of full posterior distributions  $p(\boldsymbol{\theta}|\mathbf{x}_0)$ , that is all the probable parameters that could represent the underlying tissue, along with an uncertainty measure and the interdependency of parameters. These posteriors can help interpreting the obtained results and make more informed decisions.

#### 2.1.2 The Bayesian formalism.

The posterior distribution can be defined using Bayes' theorem as follows:

$$p(\boldsymbol{\theta}|\mathbf{x}_0) = \frac{p(\mathbf{x}_0|\boldsymbol{\theta}) p(\boldsymbol{\theta})}{p(\mathbf{x}_0)} , \quad (1)$$

where  $p(\mathbf{x}_0|\boldsymbol{\theta})$  is the likelihood of the observed data point,  $p(\boldsymbol{\theta})$  is the prior distribution defining our initial knowledge of the parameter values, and  $p(\mathbf{x}_0)$  is a normalizing constant, commonly referred to as the evidence of the data.

The evidence term is usually very hard to estimate, as it corresponds to all the possible realisations of  $\mathbf{x}_0$ , i.e.  $p(\mathbf{x}_0) = \int_{all \mathbf{x}_0} p(\mathbf{x}_0|\boldsymbol{\theta}) p(\boldsymbol{\theta}) d\mathbf{x}_0$ . For simplification, methods usually estimate an unnormalized probability density function, i.e.

$$p(\boldsymbol{\theta}|\mathbf{x}_0) \propto p(\mathbf{x}_0|\boldsymbol{\theta})p(\boldsymbol{\theta}) . \quad (2)$$

An analytical expression of the likelihood distribution is often hard to write for data points generated by complex non-linear models, making difficult the use of Eq. (2). Models that do

not admit a tractable likelihood are called *implicit models* [Diggle and Gratton]. Three main approaches have then been developed to allow for the estimation of this posterior distribution: either by approximating the likelihood distribution [Papamakarios et al., c, Lueckmann et al., a], the likelihood-ratio [Cranmer et al., b, Gutmann et al., Hermans et al.] or by learning directly the posterior distribution [Papamakarios and Murray, Lueckmann et al., c, Papamakarios et al., c] using a conditional density estimator. While this work focuses on the estimate of the posterior distribution using a conditional density estimator, we show a comparison with MCMC, which are commonly used methods in the community. We will therefore introduce this method in the following paragraph.

### 2.1.3 Estimating the likelihood function.

Well-established approaches for estimating the likelihood function are MCMC methods. These methods rely on a noise model to define the likelihood distribution, such as the Rician [Panagiotaki et al., a] or Offset Gaussian models [Alexander, b]. In this work, we will be using the Microstructure Diffusion Toolbox to perform the MCMC computations [Harms and Roebroek], which relies on the Offset Gaussian model. The log-likelihood function is then the following:

$$\log(p(\mathbf{x}_0|\boldsymbol{\theta})) = -\frac{\sum (\mathbf{x}_0 - \sqrt{\mathcal{M}(\boldsymbol{\theta})^2 + \sigma^2})^2}{2\sigma^2} - m \cdot \log(\sigma\sqrt{2\pi}) , \quad (3)$$

where  $\mathcal{M}(\boldsymbol{\theta})$  is the signal obtained using the biophysical model,  $\sigma$  is the standard deviation of the Gaussian distributed noise, estimated from the reconstructed magnitude images [Dietrich et al.], and  $m$  is the number of observations in the dataset.

MCMC methods allow to obtain posterior distributions using Bayes' formula (Eq. (2)) with the previously defined likelihood function (Eq. (3)) and some prior distributions, which are usually uniform distributions defined on biologically plausible ranges. They generate a multi-dimensional chain of samples which is guaranteed to converge towards a stationary distribution, which approximates the posterior distribution [Metropolis et al., Hastings].

The need to compute the signal following the forward model at each iteration makes these sampling methods computationally expensive and time consuming. In addition, they require some adjustments specific to each model, such as the choice of burn-in length, thinning and the number of samples to store. Harms and Roebroek recommend to use the Adaptive Metropolis-Within-Gibbs (AMWG) algorithm for sampling dMRI models, initialized with a maximum likelihood estimator obtained from non-linear optimization, with 100 to 200 samples for burn-in and no thinning. The recommended number of samples is model-dependent. Authors recommendations can be found in their paper.

### 2.1.4 Bypassing the likelihood function.

An alternative method was proposed to overcome the challenges associated with approximating the likelihood function and the limitations of MCMC sampling algorithms. This approach involves directly approximating the posterior distribution by using a conditional density estimator, i.e. a family of conditional probability density function approximators denoted as  $q_\phi(\boldsymbol{\theta}|\mathbf{x})$ . These approximators are parameterized by  $\phi$  and accept both the parameters  $\boldsymbol{\theta}$  and the observation  $\mathbf{x}$  as input arguments. Our posterior approximation is then obtained by minimizing its average Kullback-Leibler divergence with respect to the conditional density estimator for different choices of  $\mathbf{x}$ , as per [Papamakarios and Murray]:

$$\min_{\phi} \mathcal{L}(\phi) \quad \text{with} \quad \mathcal{L}(\phi) = \mathbb{E}_{\mathbf{x} \sim p(\mathbf{x})} [D_{\text{KL}}(p(\boldsymbol{\theta}|\mathbf{x})||q_\phi(\boldsymbol{\theta}|\mathbf{x}))] , \quad (4)$$

which can be rewritten as

$$\begin{aligned} \mathcal{L}(\phi) &= \int D_{\text{KL}}(p(\boldsymbol{\theta}|\mathbf{x})||q_\phi(\boldsymbol{\theta}|\mathbf{x}))p(\mathbf{x})d\mathbf{x} , \\ &= -\int \int \log(q_\phi(\boldsymbol{\theta}|\mathbf{x}))p(\boldsymbol{\theta}|\mathbf{x})p(\mathbf{x})d\boldsymbol{\theta}d\mathbf{x} + C , \\ &= -\int \int \log(q_\phi(\boldsymbol{\theta}|\mathbf{x}))p(\mathbf{x}, \boldsymbol{\theta})d\boldsymbol{\theta}d\mathbf{x} + C , \\ &= -\mathbb{E}_{(\mathbf{x}, \boldsymbol{\theta}) \sim p(\mathbf{x}, \boldsymbol{\theta})} [\log(q_\phi(\boldsymbol{\theta}|\mathbf{x}))] + C , \end{aligned} \quad (5)$$

where  $C$  is a constant that does not depend on  $\phi$ . Note that in practice we consider a  $N$ -sample Monte-Carlo approximation of the loss function:

$$\mathcal{L}(\phi) \approx \mathcal{L}^N(\phi) = -\frac{1}{N} \sum_{i=1}^N \log \left( q_\phi(\boldsymbol{\theta}_i | \mathbf{x}_i) \right), \quad (6)$$

where the  $N$  data points  $(\boldsymbol{\theta}_i, \mathbf{x}_i)$  are sampled from the joint distribution with  $\boldsymbol{\theta}_i \sim p(\boldsymbol{\theta})$  and  $\mathbf{x}_i \sim p(\mathbf{x} | \boldsymbol{\theta}_i)$ . We can then use stochastic gradient descent to obtain a set of parameters  $\phi$  which minimizes  $\mathcal{L}^N$ .

If the class of conditional density estimators is sufficiently expressive, it can be demonstrated that the minimizer of Eq. (6) converges to  $p(\boldsymbol{\theta} | \mathbf{y})$  when  $N \rightarrow \infty$  [Greenberg et al.]. It is worth noting that the parametrization  $\phi$ , obtained at the end of the optimization procedure, serves as an amortized posterior for various choices of  $\mathbf{x}$ . Hence, for a particular observation  $\mathbf{x}_0$ , we can simply use  $q_\phi(\boldsymbol{\theta} | \mathbf{x}_0)$  as an approximation of  $p(\boldsymbol{\theta} | \mathbf{x}_0)$ .

## 3 Methods

### 3.1 $\mu$ GUIDE

The full architecture of the proposed Bayesian framework, dubbed  $\mu$ GUIDE, is presented in Figure 1. An open-source package for  $\mu$ GUIDE is available at: <https://github.com/mjallais/uGUIDE> (both CPU and GPU are supported).

$\mu$ GUIDE is comprised of two modules that are optimized together to minimize the Kullback–Leibler divergence between the true posterior distribution and the estimated one for every parameters of a given forward model. The ‘Neural Posterior Estimator’ (NPE) module uses normalizing flows to approximate the posterior distribution, while the ‘Multi-Layer Perceptron’ (MLP) module is used to reduce the data dimensionality and ensure fast and robust convergence of the NPE module. The following Sections provide more details about our implementation of each module.

#### 3.1.1 Neural Posterior Estimator

In this study, the Sequential Neural Posterior Estimation (SNPE-C) algorithm [Papamakarios and Murray, Greenberg et al.] is employed to train a neural network that directly approximates the posterior distribution. Thus, sampling from the posterior can be done by sampling from the trained neural network. Neural density estimators have the advantage of providing exact density evaluations, in contrast to Variational Autoencoders (VAE [Kingma and Welling]) or generative adversarial networks (GAN [Goodfellow et al.]), which are better suited for generating synthetic data.

The conditional probability density function approximators used in this project belong to a class of neural networks called normalizing flows [Papamakarios et al., a]. These flows are invertible functions capable of transforming vectors generated from a simple base distribution (e.g. the standard multivariate Gaussian distribution) into an approximation of the true posterior distribution. An autoregressive architecture for normalizing flows is employed, implemented via the Masked Autoregressive Flow (MAF [Papamakarios et al., b]), which is constructed by stacking five Masked Autoencoder for Distribution Estimation models (MADE [Germain et al.]).

#### 3.1.2 Handling the large dimensionality of the data with Multi-Layer Perceptron

As the dimensionality of the input data  $\mathbf{x}$  grows, the complexity of the corresponding inverse problem also increases. Accurately characterizing the posterior distributions or estimating the tissue microstructure parameters becomes more challenging. As a consequence, it is often necessary to rely on a set of low-dimensional features (or summary statistics) instead of the raw data for the inference task process [Blum et al., Fearnhead and Prangle, Sisson et al., Papamakarios et al., c, Chen et al.]. Learning a set of sufficient statistics before estimating the posterior distribution makes the inference easier and offers many benefits (see e.g. the Rao-Blackwell theorem).

A follow-up challenge lies in the choice of suitable summary statistics. For well-understood problems and data, it is possible to manually design these features using deterministic functions that condense the information contained in the raw signal into a set of handful summary statistics. Previous works, such as [Novikov et al., b] and [Jallais et al., b], have proposed specific summary

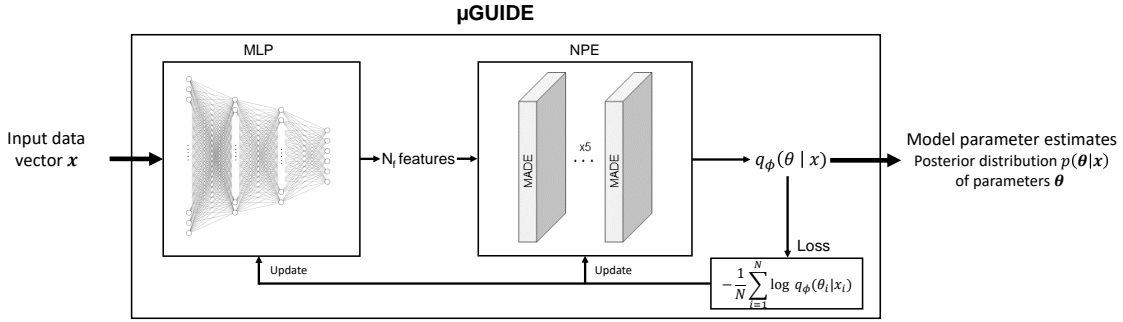


Figure 1:  $\mu$ GUIDE architecture. Input: an observed data vector. Output: a posterior distribution of the model parameters. Based on a SBI framework, it combines a Multi-Layer Perceptron (MLP) with 3 layers and a Neural Posterior Estimator (NPE). The MLP learns a low-dimensional representation of  $\mathbf{x}$ , based on a small number of features ( $N_f$ ), that can be either defined a priori or determined empirically during training. The MLP is trained simultaneously with the NPE, leading to the extraction of the optimal features that minimize the bias and uncertainty of  $p(\boldsymbol{\theta}|\mathbf{x})$ .

statistics for two different biophysical models. However, defining these summary statistics is difficult and often requires prior knowledge of the problem at hand. In the context of dMRI, they also rely on acquisition constraints and are model-specific.

In this work, the proposed framework aims to be applicable to any forward model and be as general as possible. We therefore propose to learn the summary statistics from the high-dimensional input signals  $\mathbf{x}$  using a neural network. This neural network is referred to as an embedding neural network. The observed signals are fed into the embedding neural network, whose outputs are then passed to the neural density estimator. The parameters of the embedding network are learned together with the parameters of the neural density estimator, leading to the extraction of optimal features that minimize the uncertainty of  $p(\boldsymbol{\theta}|\mathbf{x})$ . Here, we propose to use a MLP with three layers as a summary statistics extractor. The number of features  $N_f$  extracted by the MLP can be either defined a priori or determined empirically during training.

### 3.1.3 Training $\mu$ GUIDE

To train  $\mu$ GUIDE we need couples of input vectors  $\mathbf{x}$  and corresponding ground-truth values for the model parameters that we want to estimate,  $\boldsymbol{\theta}$ . The input  $\mathbf{x}$  can be real or simulated data (e.g. dMRI signals); or a mixture of these two. We train  $\mu$ GUIDE by stochastically minimizing the loss function defined in Eq. (6) using the Adam optimizer [Kingma and Ba] with a learning rate of  $10^{-3}$  and a minibatch size of 128. We use 1 million simulations for each model, 5% of which are randomly selected to be used as a validation set. Training is stopped when the validation loss does not decrease for 30 consecutive epochs.

### 3.1.4 Quantifying the confidence in the estimates

The full posterior distribution contains a lot of useful information about a given model parameter best estimates; uncertainty; ambiguity and degeneracy. To summarize and easily visualize this information, we propose three measures that quantify the best estimates and the associated confidence levels, and a way to highlight degeneracy.

We start by checking whether a posterior distribution is degenerate, that is if the distribution presents multiple distinct parameter solutions, appearing as multiple local maxima. To that aim, we fit two Gaussian distributions to the obtained posterior distributions. A voxel is considered as degenerate if the derivative of the fitted Gaussian distributions changes signs more than once (i.e. multiple local maxima), and if the two Gaussian distributions are not overlapping (the distance between the two Gaussian means is inferior to the sum of their standard deviations).

For non-degenerate posterior distributions, we extract three quantities:

1. The Maximum A Posteriori (MAP), which corresponds to the most likely parameter estimate.
2. An uncertainty measure, which quantifies the dispersion of the 50% most probable samples using the interquartile range, relative to the prior range.
3. An ambiguity measure, which measures the Full Width at Half Maximum (FWHM), in percentage with respect to the prior range.

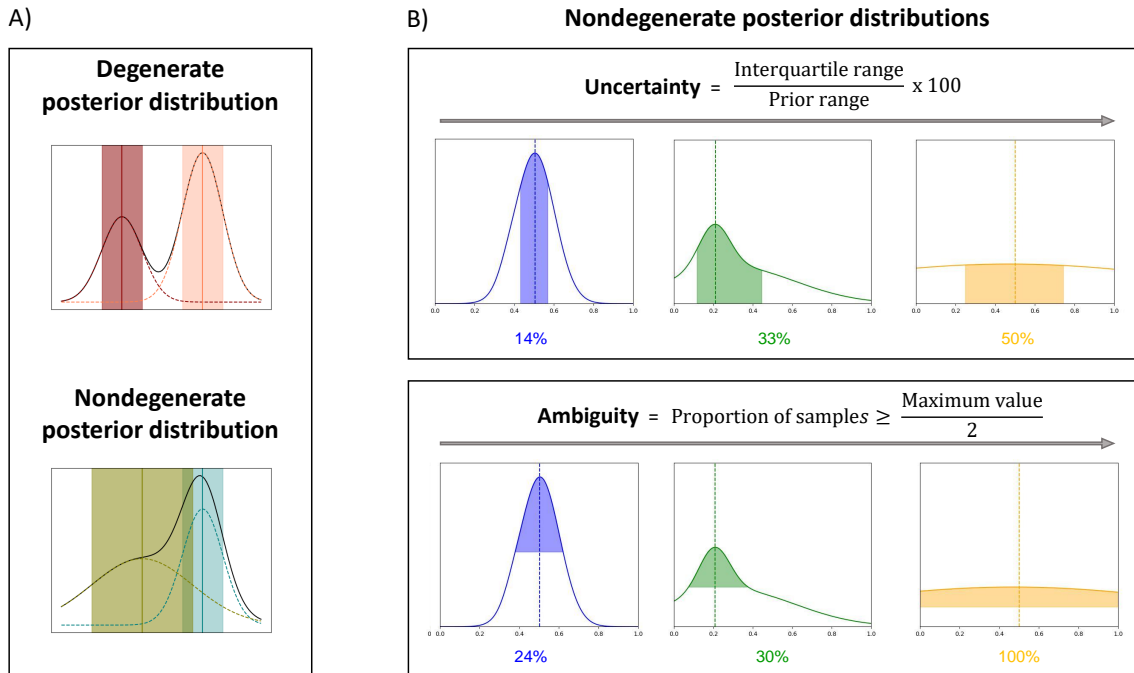


Figure 2: A) Examples of degenerate and non-degenerate posterior distributions. B) Presentation of the measures introduced to quantify a posterior distribution on exemplar non-degenerate posterior distributions. Maximum A Posteriori (MAP): is the most likely parameter estimate (dashed vertical lines). Uncertainty: measures the dispersion of the 50% most probable samples using the interquartile range, with respect to the prior range. Ambiguity: measures the Full Width at Half Maximum (FWHM), in percentage with respect to the prior range.

Figure 2 presents those measures on exemplar posterior distributions.

### 3.2 Application of $\mu$ GUIDE to biophysical modelling of dMRI data

We show exemplar applications of  $\mu$ GUIDE to three biophysical models of increasing complexity and degeneracy from the dMRI literature. For each model, we compare the fitting quality of the posterior distributions obtained using the MLP and manually defined summary statistics.

#### 3.2.1 Biophysical models of dMRI signal

**Model 1: Ball&Stick [Behrens et al.].** This is a two-compartment model (intra-neurite and extra-neurite space) where the dMRI signal from the brain tissue is modeled as a weighted sum, with weight  $f_{in}$ , of signals from water diffusing inside the neurites, approximated as sticks (i.e. cylinders of zero radius) with diffusivity  $D_{in}$ , and water diffusing within the extra-neurite space, approximated as Gaussian diffusion in an isotropic medium with diffusivity  $D_e$ . The direction of the stick is randomly sampled on a sphere. This model has the main advantage of being non-degenerate. We define the summary statistics as the direction-averaged signal (six b-shells, see section 3.2.3).

**Model 2: Standard Model (SM) [Novikov et al., a].** Expanding on model 1, this model represents the dMRI signal from the brain tissue as a weighted sum of the signal from water diffusing within the neurite space, approximated as sticks with symmetric orientation dispersion following a Watson distribution and water diffusing within the extra-neurite space, modelled as anisotropic Gaussian diffusion. The microstructure parameters of this two-compartment model are the neurite signal fraction  $f$ , the intra-neurite diffusivity  $D_a$ , the orientation dispersion index  $ODI$ , and the parallel and perpendicular diffusivities within the extra-neurite space  $D_e^{\parallel}$  and  $D_e^{\perp}$ . We use the LEMONADE [Novikov et al., b] system of equations, which is based on a cumulant decomposition of the signal, to define six summary statistics.

**Model 3: extended-SANDI [Palombo et al., a].** This is a three-compartment model (intra-neurite, intra-soma and extra-cellular space) where the dMRI signal from the brain tissue is modelled as a weighted sum of the signal from water diffusing within the neurite space, approximated as sticks with symmetric orientation dispersion following a Watson distribution; water diffusing

within cell bodies (namely soma), modelled as restricted diffusion in spheres; and water diffusing within the extra-cellular space, modelled as isotropic Gaussian diffusion. The parameters of interest are the neurite signal fraction  $f_n$ , the intra-neurite diffusivity  $D_n$ , the orientation dispersion index  $ODI$ , the extra-cellular signal fraction  $f_e$  and isotropic diffusivity  $D_e$ , the soma signal fraction  $f_s$ , and a proxy of soma radius and diffusivity  $C_s$ , defined as [Jallais et al., b]:

$$C_s = \frac{2}{D_s \delta^2} \sum_{m=1}^{\infty} \frac{\alpha_m^{-4}}{\alpha_m^2 r_s^2 - 2} \cdot \left( 2\delta - \frac{2 + e^{-\alpha_m^2 D_s (\Delta - \delta)} - e^{-\alpha_m^2 D_s \delta} - e^{-\alpha_m^2 D_s \Delta} + e^{-\alpha_m^2 D_s (\Delta + \delta)}}{\alpha_m^2 D_s} \right),$$

with  $r_s$  and  $D_s$  the soma radius and diffusivity respectively, and  $\alpha_m$  the  $m$ th root of  $(\alpha r_s)^{-1} J_{\frac{3}{2}}(\alpha r_s) = J_{\frac{5}{2}}(\alpha r_s)$ , with  $J_n(x)$  the Bessel functions of the first kind. We use the six summary statistics defined in [Jallais et al., b], which are based on a high and low b-value signal expansion.

Prior distributions  $p(\theta)$  are defined as uniform distributions over biophysically plausible ranges. Signal fractions are defined within the interval  $[0, 1]$ , diffusivities between  $0.1$  and  $3 \mu\text{m}^2 \text{ms}^{-1}$ , ODI between  $0.03$  and  $0.95$ , and  $C_s$  between  $0.15$  and  $1105 \mu\text{m}^2$  (which correspond to  $r_s \in [1; 15] \mu\text{m}$  and fixed  $D_s = 3 \mu\text{m}^2 \text{ms}^{-1}$ ).

The SM imposes the constraint  $D_e^\perp < D_e^\parallel$ . To generate samples uniformly distributed on the space defined by this condition, we are using two random variables  $u_0$  and  $u_1$ , both sampled uniformly between  $0$  and  $1$ , and then relate them to  $D_e^\parallel$  and  $D_e^\perp$  using the following equations:

$$\begin{cases} D_e^\parallel = \sqrt{(3.0 - 0.1)^2 \cdot u_0} + 0.1 \\ D_e^\perp = (D_e^\parallel - 0.1) \cdot u_1 + 0.1 \end{cases} \quad (7)$$

The extended-SANDI model requires for the signal fractions to sum to 1, that is  $f_n + f_s + f_e = 1$ . To uniformly cover the simplex  $f_n + f_s + f_e = 1$ , we define two new parameters  $k_1$  and  $k_2$ , uniformly sampled between  $0$  and  $1$ , and use the following equations to get the corresponding signal fractions:

$$\begin{cases} f_n = k_2 \sqrt{k_1} \\ f_s = (1 - k_2) \sqrt{k_1} \\ f_e = 1 - \sqrt{k_1} \end{cases} \quad (8)$$

To ensure comparability of results, we extract the same number of features  $N_f$  using the MLP as the number of summary statistics for each model. We therefore use  $N_f = 6$  for the Ball&Stick, the SM and the extended-SANDI models.

### 3.2.2 Validation in Numerical Simulations

We validated the obtained posterior distributions comparing them with the Adaptive Metropolis-Within-Gibbs MCMC [Roberts and Rosenthal]. We generated simulations following the same acquisition protocol as the real data (see section 3.2.3), and added Rician distributed noise with a Signal-to-Noise-Ratio (SNR) of 50. We then estimated the posterior distributions using both  $\mu\text{GUIDE}$  and the MCMC method implemented in the MDT toolbox [Harms and Roebroek]. We initialized the sampling using a maximum likelihood estimator. We sampled 15200 samples from the distribution, the first 200 ones being used as burn-in, and no thinning. Similarly, we sampled 15000 samples from the estimated posterior distributions using  $\mu\text{GUIDE}$ .

Then, we show that  $\mu\text{GUIDE}$  can be applicable to any model. We use model 1 and 3 as examples of simpler (and non-degenerate) and more complex (and degenerate) models than model 2, respectively.

We compared the proposed framework to a state-of-the-art method for posterior estimation [Jallais et al., b]. This method relies on manually-defined summary statistics, while  $\mu\text{GUIDE}$  automatically extracts some features using an embedded neural network.  $\mu\text{GUIDE}$  was trained directly on noisy simulations. The manually-defined summary statistics were extracted from these simulated noisy signals and then used as training dataset for a MAF, similarly to [Jallais et al., b].

Finally, we used  $\mu\text{GUIDE}$  to highlight degeneracy in all the models. While the complexity of the models increases, more degeneracy can be found. The degeneracy is inherent to the model definition, and is not induced by the noise.  $\mu\text{GUIDE}$  allows to highlight those degeneracies and quantify the confidence in the obtained estimates.

The training was performed on  $N = 10^6$  numerical simulations for each model, computed using the MISST package [Ianus et al.] and random combinations of the model parameters, each uniformly sampled from the previously defined ranges, with the addition of Rician distributed noise with SNR equivalent to the experimental data, i.e. 50.

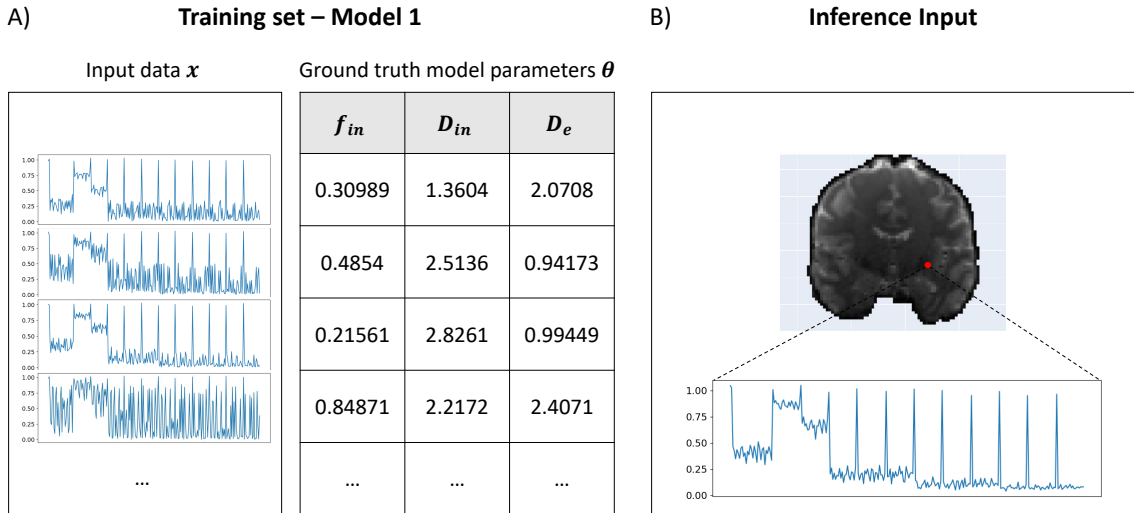


Figure 3: A) Examples of input synthetic data vectors and corresponding ground truth model parameters used in the training set of Model 1 (Ball&Stick). B) Example of input measured signals from a voxel in a healthy participant, used for inference.

### 3.2.3 dMRI Data Acquisition and Processing

We applied  $\mu$ GUIDE to dMRI data collected from two participants: a healthy volunteer from the MICRA dataset [Koller et al.] and an age-matched participant with epilepsy, acquired with the same protocol. Data were acquired on a Connectome 3T scanner using a PGSE acquisition with  $b$ -values = [200, 500, 1200, 2400, 4000, 6000] s mm<sup>-2</sup>, [20, 20, 30, 61, 61, 61] uniformly distributed directions respectively and 13 non-diffusion-weighted images at 2 mm isotropic resolution. TR was set to 3000 ms, TE to 59 ms, and the diffusion gradient duration and separation to 7 ms and 24 ms respectively. Short diffusion times and TE were achieved thanks to the Connectom gradients, allowing to enhance the signal-to-noise ratio and sensitivity to small water displacements [Jones et al., Setsompop et al.]. We considered the noise as Rician with an SNR of 50 for both subjects.

Data were preprocessed using tools from the FSL [Andersson et al., Andersson and Sotiropoulos]) and MRTrix3 [Veraart et al., b, Vos et al.] software packages. The preprocessing steps included denoising [Veraart et al., b], drift correction [Vos et al.], motion and eddy current correction [Andersson and Sotiropoulos], correction for gradient non-linearity distortions [Glasser et al.] with spatio-temporal  $b$ -value/vector tracking [Rudrapatna et al.], and Gibbs ringing artefacts correction [Kellner et al.].

### 3.2.4 dMRI Data Analysis

Diffusion signals were first normalized by the mean non-diffusion-weighted signals acquired for each voxel. Each voxel was then estimated in parallel using the  $\mu$ GUIDE framework. For each observed signal  $x_v$  (i.e. for each voxel), we drew 50000 samples via rejection-sampling from  $q_\phi(\theta_i|x_v)$  for each model parameter  $\theta_i$ , allowing to retrieve the full posterior distributions. If a posterior distribution was not deemed degenerate, the maximum-a-posteriori, uncertainty and ambiguity measures were extracted from the posterior distributions.

The manually-defined summary statistics of the SM are defined using a cumulant expansion, which is only valid for small  $b$ -values. We therefore only used the  $b \leq 2500$  s mm<sup>-2</sup> data for this model. In order to obtain comparable results, we restricted the application of  $\mu$ GUIDE to this range of  $b$ -values as well. An extra  $b$ -shell ( $b$ -value = 5000 s mm<sup>-2</sup>; 61 directions) was interpolated using *mapl* [Fick et al.] for the extended-SANDI model when using the method developed by Jallais et al. [b] based on summary statistics.

The training of  $\mu$ GUIDE was performed as described in 3.2.2 and an example of training dataset and input signal vector is provided in figure 3.

All the computations were performed both on CPU and GPU (NVIDIA GeForce RTX 4090).

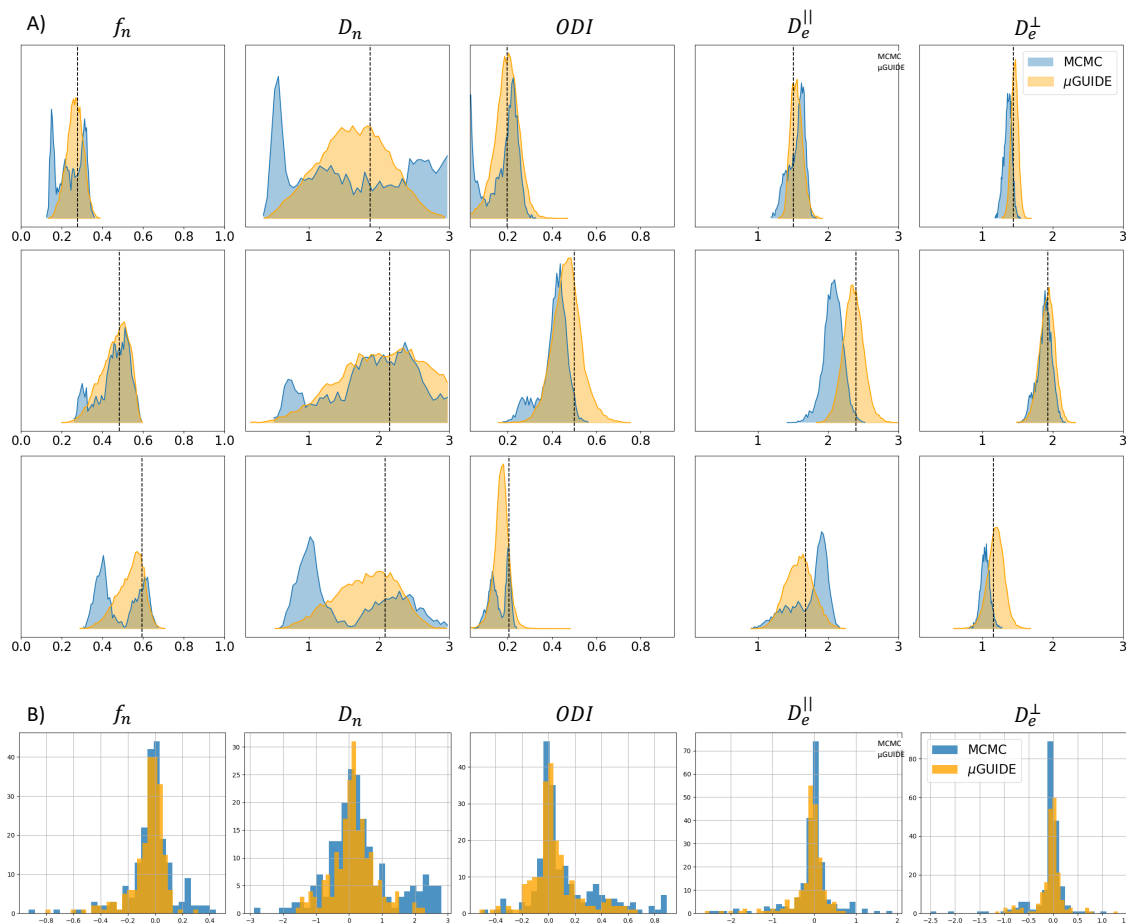


Figure 4: Comparison between  $\mu$ GUIDE and MCMC. A) Posterior distributions obtained using either  $\mu$ GUIDE or MCMC on three exemplar simulations with model 2 (SM - SNR = 50). B) Bias between the ground truth values used for simulating the diffusion signals, and the maximum-a-posteriori extracted from the posterior distributions using either  $\mu$ GUIDE or MCMC. Sharper and less biased posterior distributions are obtained using  $\mu$ GUIDE.

## 4 Results

### 4.1 Simulations

#### 4.1.1 Comparison with MCMC

We performed a comparison between the posterior distributions obtained using  $\mu$ GUIDE and MCMC, a classical Bayesian method. Figure 4A shows posterior distributions on three exemplar simulations with SNR = 50 using the model 2 (SM), obtained with 15000 samples. Sharper and less biased posterior estimations are obtained using  $\mu$ GUIDE. Figure 4B presents histograms for each model parameter of the bias between the ground truth value used to simulate a signal, and the MAP of the posterior distributions obtained with either  $\mu$ GUIDE or MCMC, on 200 simulations. Results indicate that the bias is similar or smaller using  $\mu$ GUIDE. Overall,  $\mu$ GUIDE posterior distributions are more accurate than the ones obtained with MCMC.

Moreover, it took on average 29.3 s to obtain the posterior distribution using MCMC on a GPU (NVIDIA GeForce GT 710) for one voxel, while it only took 0.02 s for  $\mu$ GUIDE.  $\mu$ GUIDE is about 1500 times faster than MCMC, which makes it more suitable for applying it on large datasets.

#### 4.1.2 The importance of feature selection

Figure 5 shows the MAP extracted from the posterior distributions versus the ground truth parameters used to generate the diffusion signal with  $\mu$ GUIDE and manually-defined summary statistics for model 1 (Ball&Stick), 2 (SM) and 3 (extended-SANDI). Less biased MAPs with lower ambiguities and uncertainties are obtained with  $\mu$ GUIDE, indicating that the MLP allows for the extraction of additional information not contained in the summary statistics, helping to solve the

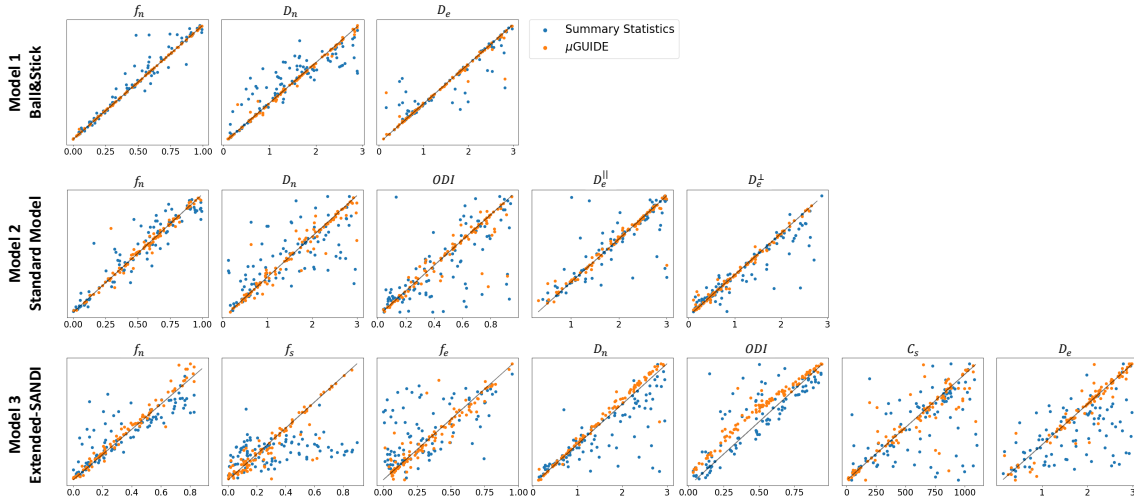


Figure 5: Maximum-A-Posteriori (MAP) extracted from the posterior distributions vs ground truth parameters used for generating the signal for the Ball&Stick, SM and extended-SANDI models. Orange points correspond to the MAPs obtained using MLP-extracted features ( $\mu$ GUIDE) and the blue ones to the MAPs with the manually-defined summary statistics. Only the non-degenerate posterior distributions have been kept. The summary statistics used in those three models are the direction-averaged signal for the Ball&Stick model, the LEMONADE system of equations [Novikov et al., b] for the SM, and the summary statistics defined in [Jallais et al., b] for the extended-SANDI model. Results are shown on 100 exemplar noise-free simulations with random parameter combinations. The optimal features extracted by the MLP allow to reduce the bias and variance of the obtained microstructure posterior distributions.

inverse problem with higher accuracy and precision.  $\mu$ GUIDE generalizes the method developed in [Jallais et al., b] to make it applicable to any forward model and any acquisition protocol, while making the estimates more precise and accurate thanks to the automatic feature extraction.

#### 4.1.3 $\mu$ GUIDE highlights degeneracies

Figure 6 presents the posterior distributions of microstructure parameters for the Ball&Stick, Standard Model and the extended-SANDI models obtained with  $\mu$ GUIDE on exemplar noise-free simulations. Blue curves correspond to non-degenerate posterior distributions, while the red ones present at least one degeneracy for one of the parameters. As the complexity of the model increases, degeneracy in the model definitions appear. This figure showcases  $\mu$ GUIDE ability to highlight degeneracy in the model parameter estimation.

Tables 1 and 2 present the number of degenerate cases for each parameter in the three models, on 10000 simulations. Table 1 considers noise-free simulations and the training and estimations were performed on CPU. Table 2 reports results on noisy simulations (Rician noise with SNR = 50), with training and testing performed on a GPU. The time needed for the inference and to estimate the posterior distributions on 10000 simulations, define if they are degenerate or not, and extract the MAP, uncertainty, ambiguity, are also reported.

## 4.2 Application to real data

After demonstrating that the proposed framework provides good estimates in the controlled case of simulations, we applied  $\mu$ GUIDE to both a healthy volunteer and a participant with epilepsy. The estimation of the posterior distributions is done independently for each voxel. To easily assess the values and the quality of the fitting, we are plotting the maximum-a-posterior, ambiguity and uncertainty maps, but the full posterior distributions are stored and available for all the voxels. Voxels presenting a degeneracy are highlighted with a red dot.

### 4.2.1 Healthy volunteer

We applied  $\mu$ GUIDE to a healthy volunteer, using the Ball&Stick, SM and extended-SANDI models. Figure 7 presents the parametric maps of an exemplar set of model parameters for each model,

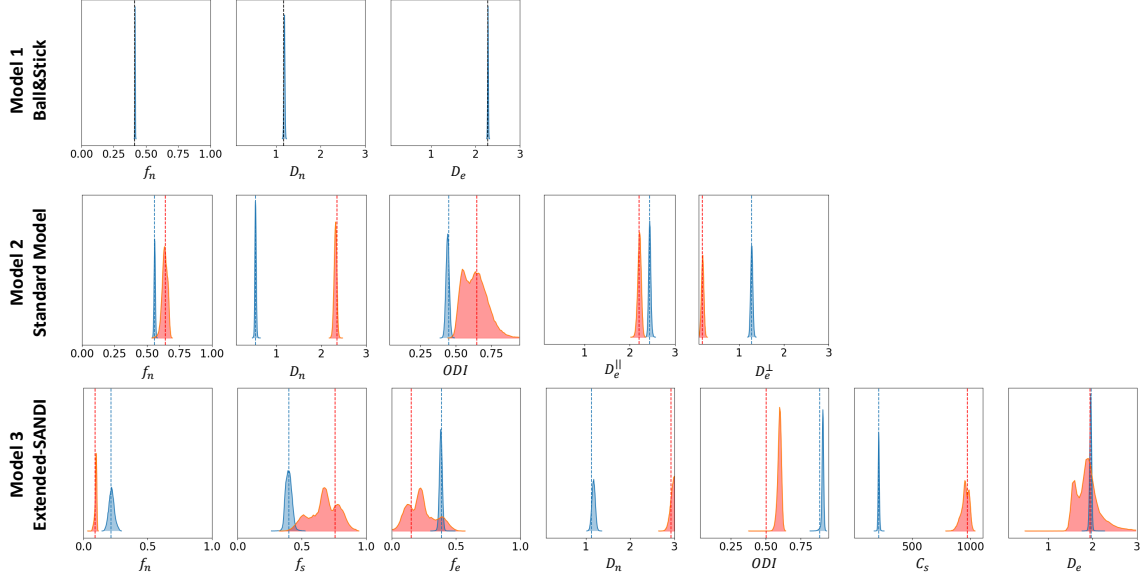


Figure 6: Posterior distributions of the microstructure parameters for the Ball&Stick, SM and extended SANDI models, obtained using  $\mu$ GUIDE on exemplar noise-free simulations. As the complexity of the model increases, degeneracies appear (red posterior distributions).  $\mu$ GUIDE allows to highlight those degeneracies present in the model definition.

Model (SNR = $\infty$ )	Training Time (CPU)	Fitting Time (on 10000 simulations)	Number of Degeneracies (on 10000 simulations)							
			$f_n$	$D_n$	$D_e^{\parallel}$	$ODI$	$D_e^{\perp}$	$f_s$	$f_e$	$C_s$
Model 1 Ball&Stick	11min	96s	0	0	0	-	-	-	-	-
Model 2 Standard Model	2h02	135s	4	34	23	33	8	-	-	-
Model 3 Extended-SANDI model	2h02	1412s	205	4	260	57	-	1395	2571	1011

Table 1: Number of degenerate cases per parameter on 10000 noise-free simulations. Training and estimations of the posterior distributions was performed on CPU. Time for training each model and time for estimating posterior distributions of 10000 noise-free simulations, define if they are degenerate or not, and extract the MAP, uncertainty, ambiguity are also reported.

Model (SNR=50)	Training Time (GPU)	Fitting Time (on 10000 simulations)	Number of Degeneracies (on 10000 simulations)							
			$f_n$	$D_n$	$D_e^{\parallel}$	$ODI$	$D_e^{\perp}$	$f_s$	$f_e$	$C_s$
Model 1 Ball&Stick	26min	79s	0	0	0	-	-	-	-	-
Model 2 Standard Model	42min	82s	75	71	117	109	29	-	-	-
Model 3 Extended-SANDI model	50min	238s	47	24	784	6	-	828	1047	56

Table 2: Number of degenerate cases per parameter on 10000 noisy simulations (Rician noise with SNR = 50). Training and estimations of the posterior distributions was performed using a GPU. Time for training each model and time for estimating posterior distributions of 10000 noisy simulations, define if they are degenerate or not, and extract the MAP, uncertainty, ambiguity are also reported.

alongside their degeneracy, uncertainty and ambiguity. The Ball&Stick model presents no degeneracy, the SM presents some degeneracy, mostly in voxels with high likelihood of partial voluming with CSF and at the white matter - gray matter boundaries. The extended-SANDI model is the model showing the highest number of degenerate cases, mostly localized within the white matter areas characterized by complex microstructure, e.g. crossing fibers. This result is expected, as the complexity of the models increases, leading to more combinations of tissue parameters that can explain an observed signal. Measures of ambiguity and uncertainty allow to quantify the confidence in the estimates and help interpreting the results.

#### 4.2.2 Participant with epilepsy

Figure 8 demonstrates  $\mu$ GUIDE application to a participant with epilepsy, using the SM. Noteworthy, the axonal signal fraction estimates within the epileptic lesion show low uncertainty and ambiguity measures hence high confidence, while orientation dispersion index estimates show high uncertainty and ambiguity suggesting low confidence, cautioning the interpretation. The two model parameters also show degeneracy in different regions of the lesion.

## 5 Discussion

### 5.1 Applicability of $\mu$ GUIDE to multiple models

The  $\mu$ GUIDE framework offers the advantage of being easily applicable to various biophysical models and representations, thanks to its data-driven approach for data reduction. The need to manually define specific summary statistics that capture the relevant information for microstructure estimation from the multi-shell diffusion signal is removed. This also eliminates the acquisition constraints that were previously imposed by the summary statistics definition [Jallais et al. \[b\]](#). The extracted features contain additional information compared to the summary statistics, resulting in a notable reduction in bias (on average 5.2 fold lower), uncertainty (on average 2.6 fold lower) and ambiguity (on average 2.7 fold lower) in the estimated posterior distributions. Consequently,  $\mu$ GUIDE improves parameters estimation over current state-of-the-art methods (e.g. [Jallais et al. \[b\]](#)), e.g., showing reduced bias (on average 5.2 fold lower) and dispersion (on average 6.4 fold lower) on the MAP estimates for each of the three example models investigated (see Fig.5).

In this study, we presented applications of  $\mu$ GUIDE to brain microstructure estimation using three well-established biophysical models, with increased complexity: the Ball&Stick model, the Standard Model, and an extended-SANDI model. However, our approach is not limited to brain tissue nor to diffusion-weighted MRI and can be extended to different organs by employing their respective acquisition encoding and forward models, such as NEXI for exchange estimates [[Jallais et al., a](#)]; mcDESPOT for myelin water fraction mapping using quantitative MRI relaxation [[Deoni et al.](#)]; VERDICT in prostate imaging [[Panagiotaki et al., b](#)]; or even adapted to different imaging modalities (e.g., EEG and MEG), where there is a way to link (via modelling or simulation) the observed signal to a set of parameters of interest. This versatility underscores the broad applicability of our proposed approach across various biological systems and imaging techniques.

It is important to note that  $\mu$ GUIDE is still a model-dependent method, meaning that the training process is based on the specific model being used. Additionally, the number of features extracted by the MLP needs to be predetermined. One way to determine the number of features is by matching it with the number of parameters being estimated. Alternatively, a dimensionality-reduction study using techniques like t-distributed stochastic neighbour embedding (tSNE) [[Van der Maaten and Hinton](#)] can be conducted to determine the optimal number of features.

### 5.2 $\mu$ GUIDE: an efficient framework for Bayesian inference

One notable advantage of  $\mu$ GUIDE is its amortized nature. With this approach, the training process is performed only once, and thereafter, the posterior estimations can be independently obtained for all voxels. This amortization enables efficient estimations of the posterior distributions.  $\mu$ GUIDE outperforms in terms of speed conventional Bayesian inference methods such as MCMC. The time savings achieved with  $\mu$ GUIDE make it a highly efficient and practical tool for estimating posterior distributions in a timely manner.

This unlocks the possibility to process with Bayesian inference very large datasets in manageable time (e.g. approximately 6 months to process 10k dMRI datasets) and to include Bayesian inference in iterative processes that require the repeated computation of the posterior distributions (e.g., dMRI acquisition optimization [[Alexander, a](#)]).

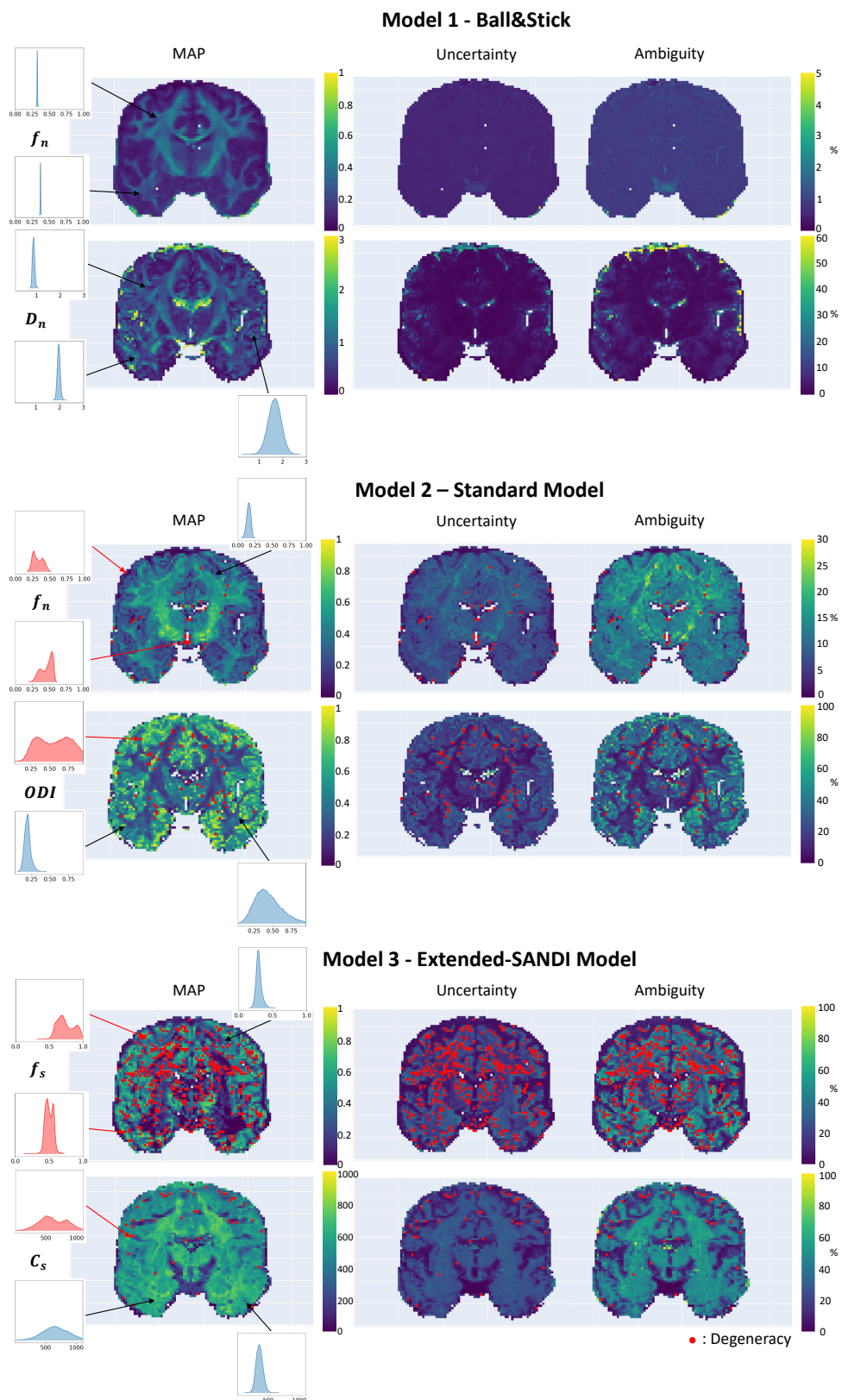


Figure 7: Parametric maps of the Ball&Stick (top), SM (middle) and extended-SANDI model (bottom), obtained using the  $\mu$ GUIDE framework: maximum-a-posteriori estimation (MAP), uncertainty and ambiguity measures, overlaid with voxels considered degenerate (red dots).

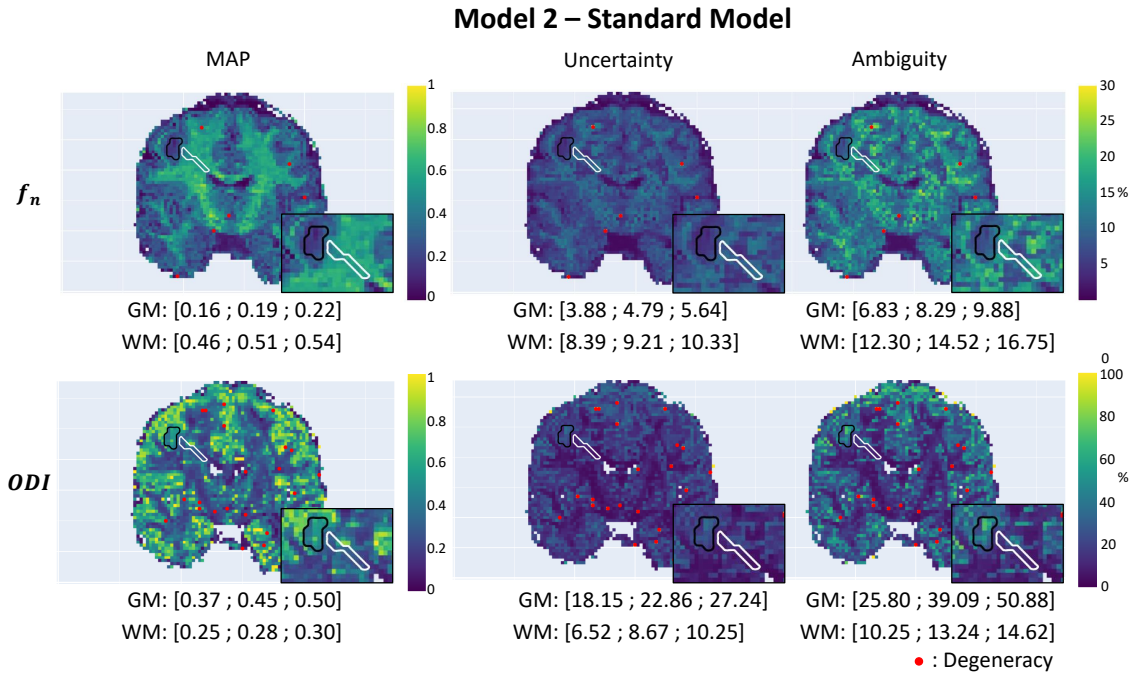


Figure 8: Parametric maps of a participant with epilepsy obtained using the  $\mu$ GUIDE framework with the SM, superimposed with the grey matter (black) and white matter (white) lesions segmentation. First quartile, mean value and third quartile of the maximum-a-posterior, uncertainty and ambiguity measures are reported in the two regions of interest. Lower MAP values are obtained in the lesions for the axonal signal fraction and the orientation dispersion index compared to healthy tissue. Higher uncertainty and ambiguity ODI values are reported, suggesting less stable estimations.

### 5.3 $\mu$ GUIDE quantifies confidence to guide interpretation

Quantifying confidence in an estimate is of crucial importance. As demonstrated by our pathological example, changes in the tissue microstructure parameters can help clinicians decide which parameters are the most reliable and better interpret microstructure changes within diseased tissue. On large population studies, the quantified uncertainty can be taken into account when performing group statistics and to detect outliers.

Variance observed in the posterior distributions can be attributed to several factors. The presence of noise in the signal contributes to irreducible variance, decreasing the confidence in the estimates as the noise level increases. Another source of variance can arise from the choice of acquisition parameters. Different acquisitions may provide varying levels of confidence in the parameter estimates. Under-sampled acquisitions or inadequate b-shells may fail to capture essential information about a tissue microstructure, such as soma or neurite radii, resulting in inaccurate estimates.

$\mu$ GUIDE can guide users in determining whether an acquisition is suitable for estimating parameters of a given model and *viceversa*, the variance and bias of the posterior distributions estimated with  $\mu$ GUIDE can be used to guide the optimization of the data acquisition to maximize accuracy and precision of the model parameters estimates.

The presence of degeneracy in the solution of the inverse problem is influenced by the complexity of the model being used and the lack of sufficient information in the data. In recent years, researchers have introduced increasingly sophisticated models to better represent the brain tissue, such as SANDI [Palombo et al., a], NEXI [Jelescu et al., a] and eSANDIX [Olesen et al.], that take into account an increasing number of tissue features. By applying  $\mu$ GUIDE, it becomes possible to gain insights into the degree of degeneracy within a model and to assess the balance between model realism and the ability to accurately invert the problem. We have recently provided an example of such application for NEXI and SANDIX [Jallais et al., a].

## 6 Conclusion

We proposed a general Bayesian framework, dubbed  $\mu$ GUIDE, to efficiently estimate posterior distributions of tissue microstructure parameters. For any given acquisition and signal model/representation,  $\mu$ GUIDE improves parameters estimation and computational time over existing state-of-the-art methods. It allows to highlight degeneracy, and quantify confidence in the estimates, guiding results interpretation towards more confident and explainable diagnosis using modern deep learning.

$\mu$ GUIDE is not inherently limited to dMRI and microstructure imaging. We envision its usage and utility to perform efficient Bayesian inference also using data from any modality where there is a way to link (via modelling or simulation) the observed measurements to a set of parameters of interest.

## Acknowledgment

This work, MJ and MP are supported by UKRI Future Leaders Fellowship (MR/T020296/2). We are thankful to Dr. Dmitri Sastin and Dr. Khalid Hamandi for sharing their dataset from a participant with epilepsy.

## References

- Maryam Afzali, Markus Nilsson, Marco Palombo, and Derek K Jones. SPHERIOUSLY? the challenges of estimating sphere radius non-invasively in the human brain from diffusion MRI. 237: 118183. ISSN 10538119. doi: 10.1016/j.neuroimage.2021.118183. URL <https://linkinghub.elsevier.com/retrieve/pii/S1053811921004602>.
- Daniel C. Alexander. A general framework for experiment design in diffusion MRI and its application in measuring direct tissue-microstructure features. 60(2):439–448, a. ISSN 0740-3194, 1522-2594. doi: 10.1002/mrm.21646. URL <https://onlinelibrary.wiley.com/doi/10.1002/mrm.21646>.
- Daniel C. Alexander. Modelling, fitting and sampling in diffusion MRI. In David Laidlaw and Joachim Weickert, editors, *Visualization and Processing of Tensor Fields*, pages 3–20. Springer Berlin Heidelberg, b. ISBN 978-3-540-88377-7 978-3-540-88378-4. doi: 10.1007/978-3-540-88378-4\_1. URL [http://link.springer.com/10.1007/978-3-540-88378-4\\_1](http://link.springer.com/10.1007/978-3-540-88378-4_1). Series Title: Mathematics and Visualization.
- Daniel C. Alexander, Tim B. Dyrby, Markus Nilsson, and Hui Zhang. Imaging brain microstructure with diffusion MRI: practicality and applications. 32(4). ISSN 0952-3480, 1099-1492. doi: 10.1002/nbm.3841. URL <https://onlinelibrary.wiley.com/doi/10.1002/nbm.3841>.
- Jesper L.R. Andersson and Stamatios N. Sotiropoulos. An integrated approach to correction for off-resonance effects and subject movement in diffusion MR imaging. 125:1063–1078. ISSN 10538119. doi: 10.1016/j.neuroimage.2015.10.019. URL <https://linkinghub.elsevier.com/retrieve/pii/S1053811915009209>.
- Jesper L.R. Andersson, Stefan Skare, and John Ashburner. How to correct susceptibility distortions in spin-echo echo-planar images: application to diffusion tensor imaging. 20(2):870–888. ISSN 10538119. doi: 10.1016/S1053-8119(03)00336-7. URL <https://linkinghub.elsevier.com/retrieve/pii/S1053811903003367>.
- T.E.J. Behrens, M.W. Woolrich, M. Jenkinson, H. Johansen-Berg, R.G. Nunes, S. Clare, P.M. Matthews, J.M. Brady, and S.M. Smith. Characterization and propagation of uncertainty in diffusion-weighted MR imaging. 50(5):1077–1088. ISSN 0740-3194, 1522-2594. doi: 10.1002/mrm.10609. URL <http://doi.wiley.com/10.1002/mrm.10609>.
- Sean R Bittner, Agostina Palmigiano, Alex T Piet, Chunyu A Duan, Carlos D Brody, Kenneth D Miller, and John Cunningham. Interrogating theoretical models of neural computation with emergent property inference. 10:e56265. ISSN 2050-084X. doi: 10.7554/eLife.56265. URL <https://elifesciences.org/articles/56265>.
- M. G. B. Blum, M. A. Nunes, D. Prangle, and S. A. Sisson. A comparative review of dimension reduction methods in approximate bayesian computation. 28(2). ISSN 0883-4237. doi: 10.1214/12-STS406. URL <https://doi.org/10.1214/12-STS406>.

[//projecteuclid.org/journals/statistical-science/volume-28/issue-2/A-Comparative-Review-of-Dimension-Reduction-Methods-in-Approximate-Bayesian/10.1214/12-ST5406.full](http://projecteuclid.org/journals/statistical-science/volume-28/issue-2/A-Comparative-Review-of-Dimension-Reduction-Methods-in-Approximate-Bayesian/10.1214/12-ST5406.full).

- George EP Box and George C Tiao. *Bayesian inference in statistical analysis*. John Wiley & Sons.
- Yanzhi Chen, Michael U Gutmann, and Adrian Weller. Is learning summary statistics necessary for likelihood-free inference?
- SungWon Chung, Ying Lu, and Roland G. Henry. Comparison of bootstrap approaches for estimation of uncertainties of DTI parameters. 33(2):531–541. ISSN 10538119. doi: 10.1016/j.neuroimage.2006.07.001. URL <https://linkinghub.elsevier.com/retrieve/pii/S1053811906007403>.
- Kyle Cranmer, Johann Brehmer, and Gilles Louppe. The frontier of simulation-based inference. page 201912789, a. ISSN 0027-8424, 1091-6490. doi: 10.1073/pnas.1912789117. URL <http://www.pnas.org/lookup/doi/10.1073/pnas.1912789117>.
- Kyle Cranmer, Juan Pavez, and Gilles Louppe. Approximating likelihood ratios with calibrated discriminative classifiers, b. URL <http://arxiv.org/abs/1506.02169>.
- João P. De Almeida Martins, Markus Nilsson, Björn Lampinen, Marco Palombo, Peter T. While, Carl-Fredrik Westin, and Filip Szczepankiewicz. Neural networks for parameter estimation in microstructural MRI: Application to a diffusion-relaxation model of white matter. 244:118601. ISSN 10538119. doi: 10.1016/j.neuroimage.2021.118601. URL <https://linkinghub.elsevier.com/retrieve/pii/S1053811921008740>.
- Sean CL Deoni, Brian K Rutt, Tarunya Arun, Carlo Pierpaoli, and Derek K Jones. Gleaning multicomponent t1 and t2 information from steady-state imaging data. 60(6):1372–1387. Publisher: Wiley Online Library.
- Olaf Dietrich, José G. Raya, Scott B. Reeder, Maximilian F. Reiser, and Stefan O. Schoenberg. Measurement of signal-to-noise ratios in MR images: Influence of multichannel coils, parallel imaging, and reconstruction filters. 26(2):375–385. ISSN 10531807, 15222586. doi: 10.1002/jmri.20969. URL <https://onlinelibrary.wiley.com/doi/10.1002/jmri.20969>.
- Peter J. Diggle and Richard J. Gratton. Monte carlo methods of inference for implicit statistical models. 46(2):193–212. ISSN 00359246. doi: 10.1111/j.2517-6161.1984.tb01290.x. URL <https://onlinelibrary.wiley.com/doi/10.1111/j.2517-6161.1984.tb01290.x>.
- Paul Fearnhead and Dennis Prangle. Constructing summary statistics for approximate bayesian computation: Semi-automatic approximate bayesian computation. 74(3):419–474. ISSN 1369-7412, 1467-9868. doi: 10.1111/j.1467-9868.2011.01010.x. URL <https://academic.oup.com/jrsssb/article/74/3/419/7075312>.
- Rutger H.J. Fick, Demian Wassermann, Emmanuel Caruyer, and Rachid Deriche. MAPL: Tissue microstructure estimation using laplacian-regularized MAP-MRI and its application to HCP data. 134:365–385. ISSN 10538119. doi: 10.1016/j.neuroimage.2016.03.046. URL <https://linkinghub.elsevier.com/retrieve/pii/S1053811916002512>.
- Els Fieremans, Jens H. Jensen, and Joseph A. Helpert. White matter characterization with diffusional kurtosis imaging. 58(1):177–188, a. ISSN 10538119. doi: 10.1016/j.neuroimage.2011.06.006. URL <https://linkinghub.elsevier.com/retrieve/pii/S1053811911006148>.
- Els Fieremans, Dmitry S. Novikov, Jens H. Jensen, and Joseph A. Helpert. Monte carlo study of a two-compartment exchange model of diffusion. 23(7):711–724, b. ISSN 09523480. doi: 10.1002/nbm.1577. URL <https://onlinelibrary.wiley.com/doi/10.1002/nbm.1577>.
- Dani Gamerman and Hedibert F Lopes. *Markov chain Monte Carlo: stochastic simulation for Bayesian inference*. CRC press.
- Mathieu Germain, Karol Gregor, Iain Murray, and Hugo Larochelle. MADE: Masked autoencoder for distribution estimation. page 9.
- Walter R Gilks, Sylvia Richardson, and David Spiegelhalter. *Markov chain Monte Carlo in practice*. CRC press.

- Matthew F. Glasser, Stamatios N. Sotiropoulos, J. Anthony Wilson, Timothy S. Coalson, Bruce Fischl, Jesper L. Andersson, Junqian Xu, Saad Jbabdi, Matthew Webster, Jonathan R. Polimeni, David C. Van Essen, and Mark Jenkinson. The minimal preprocessing pipelines for the human connectome project. 80:105–124. ISSN 10538119. doi: 10.1016/j.neuroimage.2013.04.127. URL <https://linkinghub.elsevier.com/retrieve/pii/S1053811913005053>.
- Ting Gong, Qiqi Tong, Hongjian He, Yi Sun, Jianhui Zhong, and Hui Zhang. MTE-NODDI: Multi-TE NODDI for disentangling non-t2-weighted signal fractions from compartment-specific t2 relaxation times. 217:116906. ISSN 10538119. doi: 10.1016/j.neuroimage.2020.116906. URL <https://linkinghub.elsevier.com/retrieve/pii/S105381192030392X>.
- Pedro J Gonçalves, Jan-Matthis Lueckmann, Michael Deistler, Marcel Nonnenmacher, Kaan Öcal, Giacomo Bassetto, Chaitanya Chintaluri, William F Podlaski, Sara A Haddad, Tim P Vogels, David S Greenberg, and Jakob H Macke. Training deep neural density estimators to identify mechanistic models of neural dynamics. 9:e56261. ISSN 2050-084X. doi: 10.7554/eLife.56261. URL <https://elifesciences.org/articles/56261>.
- Ian J. Goodfellow, Jean Pouget-Abadie, Mehdi Mirza, Bing Xu, David Warde-Farley, Sherjil Ozair, Aaron Courville, and Yoshua Bengio. Generative adversarial networks. URL <http://arxiv.org/abs/1406.2661>.
- David S. Greenberg, Marcel Nonnenmacher, and Jakob H. Macke. Automatic posterior transformation for likelihood-free inference. URL <http://arxiv.org/abs/1905.07488>.
- Michele Guerreri, Sean Epstein, Hojjat Azadbakht, and Hui Zhang. Resolving quantitative MRI model degeneracy with machine learning via training data distribution design. URL <http://arxiv.org/abs/2303.05464>.
- Michael U. Gutmann, Ritabrata Dutta, Samuel Kaski, and Jukka Corander. Likelihood-free inference via classification. 28(2):411–425. ISSN 0960-3174, 1573-1375. doi: 10.1007/s11222-017-9738-6. URL <http://link.springer.com/10.1007/s11222-017-9738-6>.
- Noemi G. Gyori, Marco Palombo, Christopher A. Clark, Hui Zhang, and Daniel C. Alexander. Training data distribution significantly impacts the estimation of tissue microstructure with machine learning. 87(2):932–947. ISSN 0740-3194, 1522-2594. doi: 10.1002/mrm.29014. URL <https://onlinelibrary.wiley.com/doi/10.1002/mrm.29014>.
- Robbert L. Harms and Alard Roebroeck. Robust and fast markov chain monte carlo sampling of diffusion MRI microstructure models. 12:97. ISSN 1662-5196. doi: 10.3389/fninf.2018.00097. URL <https://www.frontiersin.org/article/10.3389/fninf.2018.00097/full>.
- W. K. Hastings. Monte carlo sampling methods using markov chains and their applications. 57(1):97–109. ISSN 0006-3444. doi: 10.1093/biomet/57.1.97. URL <https://doi.org/10.1093/biomet/57.1.97>. eprint: <https://academic.oup.com/biomet/article-pdf/57/1/97/23940249/57-1-97.pdf>.
- Rafael N. Henriques, Marco Palombo, Sune N. Jespersen, Noam Shemesh, Henrik Lundell, and Andrada Ianuş. Double diffusion encoding and applications for biomedical imaging. 348:108989. ISSN 01650270. doi: 10.1016/j.jneumeth.2020.108989. URL <https://linkinghub.elsevier.com/retrieve/pii/S016502702030412X>.
- Joeri Hermans, Volodimir Begy, and Gilles Louppe. Likelihood-free MCMC with amortized approximate ratio estimators.
- Amy Fd Howard, Michiel Cottaar, Mark Drakesmith, Qiuyun Fan, Susie Y. Huang, Derek K. Jones, Frederik J. Lange, Jeroen Mollink, Suryanarayana Umesh Rudrapatna, Qiyuan Tian, Karla L Miller, and Saad Jbabdi. Estimating axial diffusivity in the NODDI model. 262:119535. ISSN 10538119. doi: 10.1016/j.neuroimage.2022.119535. URL <https://linkinghub.elsevier.com/retrieve/pii/S1053811922006504>.
- Andrada Ianuş, Noam Shemesh, Daniel C. Alexander, and Ivana Drobnjak. Double oscillating diffusion encoding and sensitivity to microscopic anisotropy: Double oscillating diffusion encoding. 78(2):550–564. ISSN 07403194. doi: 10.1002/mrm.26393. URL <https://onlinelibrary.wiley.com/doi/10.1002/mrm.26393>.

- Maëli Jallais, Marco Palombo, Ileana Jelescu, and Quentin Uhl. Shining light on degeneracies and uncertainties in the NEXI and SANDIX models with  $\mu$ GUIDE. In *ISMRM 2024*, a.
- Maëli Jallais, Pedro L. C. Rodrigues, Alexandre Gramfort, and Demian Wassermann. Inverting brain grey matter models with likelihood-free inference: a tool for trustable cytoarchitecture measurements. 1:1–28, b. ISSN 2766-905X. doi: <https://doi.org/10.59275/j.melba.2022-a964>. URL <https://melba-journal.org/2022:010>.
- Ileana O. Jelescu and Matthew D. Budde. Design and validation of diffusion MRI models of white matter. 5. ISSN 2296-424X. doi: 10.3389/fphy.2017.00061. URL <http://journal.frontiersin.org/article/10.3389/fphy.2017.00061/full>.
- Ileana O. Jelescu, Alexandre de Skowronski, Françoise Geffroy, Marco Palombo, and Dmitry S. Novikov. Neurite exchange imaging (NEXI): A minimal model of diffusion in gray matter with inter-compartment water exchange. 256:119277, a. ISSN 10538119. doi: 10.1016/j.neuroimage.2022.119277. URL <https://linkinghub.elsevier.com/retrieve/pii/S1053811922003986>.
- Ileana O. Jelescu, Marco Palombo, Francesca Bagnato, and Kurt G. Schilling. Challenges for biophysical modeling of microstructure. 344:108861, b. ISSN 01650270. doi: 10.1016/j.jneumeth.2020.108861. URL <https://linkinghub.elsevier.com/retrieve/pii/S0165027020302843>.
- Ileana O. Jelescu, Jelle Veraart, Els Fieremans, and Dmitry S. Novikov. Degeneracy in model parameter estimation for multi-compartmental diffusion in neuronal tissue: Degeneracy in model parameter estimation of diffusion in neural tissue. 29(1):33–47, c. ISSN 09523480. doi: 10.1002/nbm.3450. URL <http://doi.wiley.com/10.1002/nbm.3450>.
- Sune Nørhøj Jespersen, Jonas Lyng Olesen, Brian Hansen, and Noam Shemesh. Diffusion time dependence of microstructural parameters in fixed spinal cord. 182:329–342. ISSN 10538119. doi: 10.1016/j.neuroimage.2017.08.039. URL <https://linkinghub.elsevier.com/retrieve/pii/S1053811917306869>.
- Derek K. Jones. Determining and visualizing uncertainty in estimates of fiber orientation from diffusion tensor MRI. 49(1):7–12. ISSN 0740-3194, 1522-2594. doi: 10.1002/mrm.10331. URL <http://doi.wiley.com/10.1002/mrm.10331>.
- D.K. Jones, D.C. Alexander, R. Bowtell, M. Cercignani, F. Dell’Acqua, D.J. McHugh, K.L. Miller, M. Palombo, G.J.M. Parker, U.S. Rudrapatna, and C.M.W. Tax. Microstructural imaging of the human brain with a ‘super-scanner’: 10 key advantages of ultra-strong gradients for diffusion MRI. 182:8–38. ISSN 10538119. doi: 10.1016/j.neuroimage.2018.05.047. URL <https://linkinghub.elsevier.com/retrieve/pii/S1053811918304610>.
- Hazhar Sufi Karimi, Arghya Pal, Lipeng Ning, and Yogesh Rathi. Likelihood-free posterior estimation and uncertainty quantification for diffusion MRI models. ISSN 2837-6056. doi: 10.1162/imag\_a\_00088. URL [https://direct.mit.edu/imag/article/doi/10.1162/imag\\_a\\_00088/119146/Likelihood-free-Posterior-Estimation-and](https://direct.mit.edu/imag/article/doi/10.1162/imag_a_00088/119146/Likelihood-free-Posterior-Estimation-and).
- Göran Kauermann, Gerda Claeskens, and J. D. Opsomer. Bootstrapping for penalized spline regression. 18(1):126–146. ISSN 1061-8600, 1537-2715. doi: 10.1198/jcgs.2009.0008. URL <http://www.tandfonline.com/doi/abs/10.1198/jcgs.2009.0008>.
- Elias Kellner, Bibek Dhital, Valerij G. Kiselev, and Marco Reisert. Gibbs-ringing artifact removal based on local subvoxel-shifts. 76(5):1574–1581. doi: <https://doi.org/10.1002/mrm.26054>. URL <https://onlinelibrary.wiley.com/doi/abs/10.1002/mrm.26054>. eprint: <https://onlinelibrary.wiley.com/doi/pdf/10.1002/mrm.26054>.
- Diederik Kingma and Jimmy Ba. Adam: A method for stochastic optimization. In *International Conference on Learning Representations (ICLR)*.
- Diederik P. Kingma and Max Welling. An introduction to variational autoencoders. In *Foundations and Trends® in Machine Learning*, volume 12, pages 307–392. now Publishers Inc. doi: 10.1561/22000000056.
- Martin A. Koch, David G. Norris, and Margret Hund-Georgiadis. An investigation of functional and anatomical connectivity using magnetic resonance imaging. 16(1):241–250. ISSN 10538119. doi: 10.1006/nimg.2001.1052. URL <https://linkinghub.elsevier.com/retrieve/pii/S1053811901910523>.

- Kristin Koller, Umesh Rudrapatna, Maxime Chamberland, Erika P. Raven, Greg D. Parker, Chantal M.W. Tax, Mark Drakesmith, Fabrizio Fasano, David Owen, Garin Hughes, Cyril Charon, C John Evans, and Derek K. Jones. MICRA: Microstructural image compilation with repeated acquisitions. 225:117406. ISSN 10538119. doi: 10.1016/j.neuroimage.2020.117406. URL <https://linkinghub.elsevier.com/retrieve/pii/S1053811920308910>.
- Björn Lampinen, Filip Szczepankiewicz, Jimmy Lätt, Linda Knutsson, Johan Mårtensson, Isabella M. Björkman-Burtscher, Danielle Van Westen, Pia C. Sundgren, Freddy Ståhlberg, and Markus Nilsson. Probing brain tissue microstructure with MRI: principles, challenges, and the role of multidimensional diffusion-relaxation encoding. 282:120338, a. ISSN 10538119. doi: 10.1016/j.neuroimage.2023.120338. URL <https://linkinghub.elsevier.com/retrieve/pii/S1053811923004895>.
- Björn Lampinen, Filip Szczepankiewicz, Johan Mårtensson, Danielle Van Westen, Oskar Hansson, Carl-Fredrik Westin, and Markus Nilsson. Towards unconstrained compartment modeling in white matter using diffusion-relaxation MRI with tensor-valued diffusion encoding. 84(3):1605–1623, b. ISSN 0740-3194, 1522-2594. doi: 10.1002/mrm.28216. URL <https://onlinelibrary.wiley.com/doi/10.1002/mrm.28216>.
- Björn Lampinen, Filip Szczepankiewicz, Johan Mårtensson, Danielle van Westen, Pia C. Sundgren, and Markus Nilsson. Neurite density imaging versus imaging of microscopic anisotropy in diffusion MRI: A model comparison using spherical tensor encoding. 147:517–531, c. ISSN 10538119. doi: 10.1016/j.neuroimage.2016.11.053. URL <https://linkinghub.elsevier.com/retrieve/pii/S105381191630670X>.
- Björn Lampinen, Filip Szczepankiewicz, Mikael Novén, Danielle Van Westen, Oskar Hansson, Elisabet Englund, Johan Mårtensson, Carl-Fredrik Westin, and Markus Nilsson. Searching for the neurite density with diffusion MRI: Challenges for biophysical modeling. 40(8):2529–2545, d. ISSN 1065-9471, 1097-0193. doi: 10.1002/hbm.24542. URL <https://onlinelibrary.wiley.com/doi/10.1002/hbm.24542>.
- Mariana Lazar and Andrew L. Alexander. Bootstrap white matter tractography (BOOT-TRAC). 24(2):524–532. ISSN 10538119. doi: 10.1016/j.neuroimage.2004.08.050. URL <https://linkinghub.elsevier.com/retrieve/pii/S1053811904005130>.
- Jan-Matthis Lueckmann, Giacomo Bassetto, Theofanis Karaletsos, and Jakob H. Macke. Likelihood-free inference with emulator networks. In Francisco Ruiz, Cheng Zhang, Dawen Liang, and Thang Bui, editors, *Proceedings of The 1st Symposium on Advances in Approximate Bayesian Inference*, volume 96 of *Proceedings of Machine Learning Research*, pages 32–53. PMLR, a. URL <https://proceedings.mlr.press/v96/lueckmann19a.html>.
- Jan-Matthis Lueckmann, Jan Boelts, David Greenberg, Pedro Goncalves, and Jakob Macke. Benchmarking simulation-based inference. In Arindam Banerjee and Kenji Fukumizu, editors, *Proceedings of The 24th International Conference on Artificial Intelligence and Statistics*, volume 130 of *Proceedings of Machine Learning Research*, pages 343–351. PMLR, b. URL <https://proceedings.mlr.press/v130/lueckmann21a.html>.
- Jan-Matthis Lueckmann, Pedro J Goncalves, Giacomo Bassetto, Kaan Öcal, Marcel Nonnenmacher, and Jakob H Macke. Flexible statistical inference for mechanistic models of neural dynamics. In I. Guyon, U. Von Luxburg, S. Bengio, H. Wallach, R. Fergus, S. Vishwanathan, and R. Garnett, editors, *Advances in Neural Information Processing Systems*, volume 30. Curran Associates, Inc., c. URL [https://proceedings.neurips.cc/paper\\_files/paper/2017/file/addfa9b7e234254d26e9c7f2af1005cb-Paper.pdf](https://proceedings.neurips.cc/paper_files/paper/2017/file/addfa9b7e234254d26e9c7f2af1005cb-Paper.pdf).
- Nicholas Metropolis, Arianna W. Rosenbluth, Marshall N. Rosenbluth, Augusta H. Teller, and Edward Teller. Equation of state calculations by fast computing machines. 21(6):1087–1092. ISSN 0021-9606, 1089-7690. doi: 10.1063/1.1699114. URL <https://pubs.aip.org/jcp/article/21/6/1087/202680/Equation-of-State-Calculations-by-Fast-Computing>.
- Eloise Mougél, Julien Valette, and Marco Palombo. Investigating exchange, structural disorder and restriction in gray matter via water and metabolites diffusivity and kurtosis time-dependence. eprint: 2306.16984.

- Dmitry S. Novikov, Els Fieremans, Sune N. Jespersen, and Valerij G. Kiselev. Quantifying brain microstructure with diffusion MRI: Theory and parameter estimation: Brain microstructure with dMRI: Theory and parameter estimation. page e3998, a. ISSN 09523480. doi: 10.1002/nbm.3998. URL <http://doi.wiley.com/10.1002/nbm.3998>.
- Dmitry S. Novikov, Jelle Veraart, Ileana O. Jelescu, and Els Fieremans. Rotationally-invariant mapping of scalar and orientational metrics of neuronal microstructure with diffusion MRI. 174: 518–538, b. ISSN 10538119. doi: 10.1016/j.neuroimage.2018.03.006. URL <https://linkinghub.elsevier.com/retrieve/pii/S1053811918301915>.
- Jonas L. Olesen, Leif Østergaard, Noam Shemesh, and Sune N. Jespersen. Diffusion time dependence, power-law scaling, and exchange in gray matter. 251:118976. ISSN 10538119. doi: 10.1016/j.neuroimage.2022.118976. URL <https://linkinghub.elsevier.com/retrieve/pii/S1053811922001057>.
- Marco Palombo, Andrada Ianus, Michele Guerreri, Daniel Nunes, Daniel C. Alexander, Noam Shemesh, and Hui Zhang. SANDI: A compartment-based model for non-invasive apparent soma and neurite imaging by diffusion MRI. 215:116835, a. ISSN 10538119. doi: 10.1016/j.neuroimage.2020.116835. URL <https://linkinghub.elsevier.com/retrieve/pii/S1053811920303220>.
- Marco Palombo, Vanya Valindria, Saurabh Singh, Eleni Chiou, Francesco Giganti, Hayley Pye, Hayley C. Whitaker, David Atkinson, Shonit Punwani, Daniel C. Alexander, and Eleftheria Panagiotaki. Joint estimation of relaxation and diffusion tissue parameters for prostate cancer with relaxation-VERDICT MRI. 13(1):2999, b. ISSN 2045-2322. doi: 10.1038/s41598-023-30182-1. URL <https://www.nature.com/articles/s41598-023-30182-1>.
- Eleftheria Panagiotaki, Torben Schneider, Bernard Siow, Matt G. Hall, Mark F. Lythgoe, and Daniel C. Alexander. Compartment models of the diffusion MR signal in brain white matter: A taxonomy and comparison. 59(3):2241–2254, a. ISSN 10538119. doi: 10.1016/j.neuroimage.2011.09.081. URL <https://linkinghub.elsevier.com/retrieve/pii/S1053811911011566>.
- Eleftheria Panagiotaki, Simon Walker-Samuel, Bernard Siow, S. Peter Johnson, Vineeth Rajkumar, R. Barbara Pedley, Mark F. Lythgoe, and Daniel C. Alexander. Noninvasive quantification of solid tumor microstructure using VERDICT MRI. 74(7):1902–1912, b. ISSN 0008-5472, 1538-7445. doi: 10.1158/0008-5472.CAN-13-2511. URL <https://aacrjournals.org/cancerres/article/74/7/1902/599821/Noninvasive-Quantification-of-Solid-Tumor>.
- George Papamakarios and Iain Murray. Fast -free inference of simulation models with bayesian conditional density estimation.
- George Papamakarios, Eric Nalisnick, Danilo Jimenez Rezende, Shakir Mohamed, and Balaji Lakshminarayanan. Normalizing flows for probabilistic modeling and inference. a. URL <http://arxiv.org/abs/1912.02762>.
- George Papamakarios, Theo Pavlakou, and Iain Murray. Masked autoregressive flow for density estimation. b. URL <http://arxiv.org/abs/1705.07057>.
- George Papamakarios, David C Sterratt, and Iain Murray. Sequential neural likelihood: Fast likelihood-free inference with autoregressive flows. c.
- Geoff J. M. Parker and Daniel C. Alexander. Probabilistic monte carlo based mapping of cerebral connections utilising whole-brain crossing fibre information. In Chris Taylor and J. Alison Noble, editors, *Information Processing in Medical Imaging*, volume 2732, pages 684–695. Springer Berlin Heidelberg. ISBN 978-3-540-40560-3 978-3-540-45087-0. doi: 10.1007/978-3-540-45087-0\_57. URL [http://link.springer.com/10.1007/978-3-540-45087-0\\_57](http://link.springer.com/10.1007/978-3-540-45087-0_57). Series Title: Lecture Notes in Computer Science.
- Gareth O. Roberts and Jeffrey S. Rosenthal. Examples of adaptive MCMC. 18(2):349–367. ISSN 1061-8600, 1537-2715. doi: 10.1198/jcgs.2009.06134. URL <http://www.tandfonline.com/doi/abs/10.1198/jcgs.2009.06134>.
- Umesh Rudrapatna, Greg D. Parker, Jamie Roberts, and Derek K. Jones. A comparative study of gradient nonlinearity correction strategies for processing diffusion data obtained with ultra-strong gradient MRI scanners. 85(2):1104–1113. ISSN 0740-3194, 1522-2594. doi: 10.1002/mrm.28464. URL <https://onlinelibrary.wiley.com/doi/10.1002/mrm.28464>.

- K. Setsompop, R. Kimmlingen, E. Eberlein, T. Witzel, J. Cohen-Adad, J.A. McNab, B. Keil, M.D. Tisdall, P. Hoecht, P. Dietz, S.F. Cauley, V. Tountcheva, V. Matschl, V.H. Lenz, K. Heberlein, A. Potthast, H. Thein, J. Van Horn, A. Toga, F. Schmitt, D. Lehne, B.R. Rosen, V. Wedeen, and L.L. Wald. Pushing the limits of in vivo diffusion MRI for the human connectome project. 80: 220–233. ISSN 10538119. doi: 10.1016/j.neuroimage.2013.05.078. URL <https://linkinghub.elsevier.com/retrieve/pii/S1053811913005788>.
- S. A. Sisson, Y. Fan, and M. A. Beaumont. Overview of approximate bayesian computation. URL <http://arxiv.org/abs/1802.09720>.
- Paddy J. Slator, Marco Palombo, Karla L. Miller, Carl-Fredrik Westin, Frederik Laun, Daeun Kim, Justin P. Haldar, Dan Benjamini, Gregory Lemberskiy, Joao P. de Almeida Martins, and Jana Hutter. Combined diffusion-relaxometry microstructure imaging: Current status and future prospects. 86(6):2987–3011. doi: <https://doi.org/10.1002/mrm.28963>. URL <https://onlinelibrary.wiley.com/doi/abs/10.1002/mrm.28963>. eprint: <https://onlinelibrary.wiley.com/doi/pdf/10.1002/mrm.28963>.
- S. N. Sotiropoulos, S. Jbabdi, J. L. Andersson, M. W. Woolrich, K. Ugurbil, and T. E. J. Behrens. RubiX: Combining spatial resolutions for bayesian inference of crossing fibers in diffusion MRI. 32(6):969–982. ISSN 0278-0062, 1558-254X. doi: 10.1109/TMI.2012.2231873. URL <http://ieeexplore.ieee.org/document/6420959/>.
- Alvaro Tejero-Cantero, Jan Boelts, Michael Deistler, Jan-Matthis Lueckmann, Conor Durkan, Pedro J. Gonçalves, David S. Greenberg, and Jakob H. Macke. SBI – a toolkit for simulation-based inference. URL <http://arxiv.org/abs/2007.09114>.
- Quentin Uhl, Tommaso Pavan, Malwina Molendowska, Derek K. Jones, Marco Palombo, and Ileana Jelescu. Quantifying human gray matter microstructure using NEXI and 300 mT/m gradients. eprint: 2307.09492.
- Laurens Van der Maaten and Geoffrey Hinton. Visualizing data using t-SNE. 9(11).
- Jelle Veraart, Els Fieremans, and Dmitry S. Novikov. On the scaling behavior of water diffusion in human brain white matter. 185:379–387, a. ISSN 10538119. doi: 10.1016/j.neuroimage.2018.09.075. URL <https://linkinghub.elsevier.com/retrieve/pii/S1053811918319475>.
- Jelle Veraart, Dmitry S. Novikov, Daan Christiaens, Benjamin Ades-aron, Jan Sijbers, and Els Fieremans. Denoising of diffusion MRI using random matrix theory. 142:394–406, b. ISSN 10538119. doi: 10.1016/j.neuroimage.2016.08.016. URL <https://linkinghub.elsevier.com/retrieve/pii/S1053811916303949>.
- Jelle Veraart, Dmitry S. Novikov, and Els Fieremans. TE dependent diffusion imaging (TEdDI) distinguishes between compartmental t2 relaxation times. 182:360–369, c. ISSN 10538119. doi: 10.1016/j.neuroimage.2017.09.030. URL <https://linkinghub.elsevier.com/retrieve/pii/S1053811917307784>.
- Mélissa Vincent, Marco Palombo, and Julien Valette. Revisiting double diffusion encoding MRS in the mouse brain at 11.7t: Which microstructural features are we sensitive to? 207:116399. ISSN 10538119. doi: 10.1016/j.neuroimage.2019.116399. URL <https://linkinghub.elsevier.com/retrieve/pii/S1053811919309905>.
- Sjoerd B. Vos, Chantal M. W. Tax, Peter R. Luijten, Sebastien Ourselin, Alexander Leemans, and Martijn Froeling. The importance of correcting for signal drift in diffusion MRI. 77(1):285–299. ISSN 0740-3194, 1522-2594. doi: 10.1002/mrm.26124. URL <https://onlinelibrary.wiley.com/doi/10.1002/mrm.26124>.
- William Warner, Marco Palombo, Renata Cruz, Ross Callaghan, Noam Shemesh, Derek K. Jones, Flavio Dell’Acqua, Andrada Ianus, and Ivana Drobnjak. Temporal diffusion ratio (TDR) for imaging restricted diffusion: Optimisation and pre-clinical demonstration. 269:119930. ISSN 10538119. doi: 10.1016/j.neuroimage.2023.119930. URL <https://linkinghub.elsevier.com/retrieve/pii/S1053811923000782>.
- Brandon Witcher, David S. Tuch, Jonathan J. Wisco, A. Gregory Sorensen, and Liqun Wang. Using the wild bootstrap to quantify uncertainty in diffusion tensor imaging. 29(3):346–362. ISSN 10659471, 10970193. doi: 10.1002/hbm.20395. URL <https://onlinelibrary.wiley.com/doi/10.1002/hbm.20395>.

Dmitriy A. Yablonskiy and Alexander L. Sukstanskii. Theoretical models of the diffusion weighted MR signal. 23(7):661–681. ISSN 09523480. doi: 10.1002/nbm.1520. URL <http://doi.wiley.com/10.1002/nbm.1520>.

Hui Zhang, Torben Schneider, Claudia A. Wheeler-Kingshott, and Daniel C. Alexander. NODDI: Practical in vivo neurite orientation dispersion and density imaging of the human brain. 61(4): 1000–1016. ISSN 10538119. doi: 10.1016/j.neuroimage.2012.03.072. URL <https://linkinghub.elsevier.com/retrieve/pii/S1053811912003539>.